JACS
JOURNAL OF THE AMERICAN CHEMICAL SOCIETY
pubs.acs.org/JACS
Article

Li_5Sn, the Most Lithium-Rich Binary Stannide: A Combined Experimental and Computational Study

Robert U. Stelzer, Yuji Ikeda,* Prashanth Srinivasan, Tanja S. Lehmann, Blazej Grabowski, and Rainer Niewa

Cite This: *J. Am. Chem. Soc.* 2022, 144, 7096–7110
Read Online
ACCESS | Metrics & More | Article Recommendations | Supporting Information

ABSTRACT: From reaction of excess lithium with tin, we isolate well-crystallized Li_5Sn and solve the crystal structure from single-crystal X-ray diffraction data. The orthorhombic structure (space group *Cmcm*) features the same coordination polyhedra around tin and lithium as previously predicted by electronic structure calculations for this composition, however differently arranged. An extensive *ab initio* analysis, including thermodynamic integration using Langevin dynamics in combination with a machine-learning potential (moment tensor potential), is conducted to understand the thermodynamic stability of this *Cmcm* Li_5Sn structure observed in our experiments. Among the 108 Li_5Sn structures systematically derived using the structure enumeration algorithm, including the experimental *Cmcm* structure and those obtained in previous *ab initio* studies, another new structure with the space group *Immm* is found to be energetically most stable at 0 K. This computationally discovered *Immm* structure is also found to be thermodynamically more stable than the *Cmcm* structure at finite temperatures, indicating that the *Cmcm* Li_5Sn structure observed in our experiments is favored likely due to kinetic reasons rather than thermodynamics.

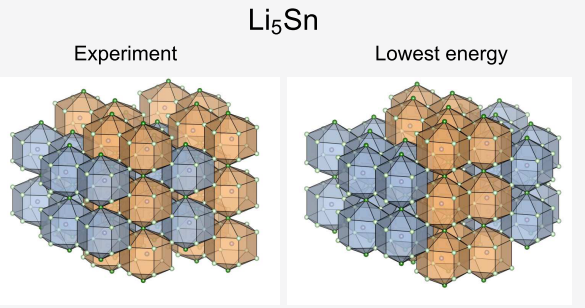

1. INTRODUCTION

Since the beginning of the 21st century, lithium ion batteries have conquered the market of portable electronic devices. However, to meet the increasing requirements of electromobility, the commercial graphite anodes with a maximum capacity of 372 mAh/g need to be replaced by materials with an increased specific lithium uptake and thus enhanced capacity.[1] Particularly the tetrels Si and Sn offer an increased storage capacity via the formation of binary intermetallic phases with Li. For Si a remarkable maximum capacity of 1978 mAh/g upon formation of $Li_{17}Si_4$ can be achieved. Sn delivers a similarly noteworthy capacity of 769 mAh/g during formation of $Li_{17}Sn_4$, though smaller than Si due to the larger relative volumes and masses. Both tetrels Si and Sn are nontoxic, comparably inexpensive, and readily available. Disadvantages are still the severe volume changes during cycling, which result in capacity losses[2] and mechanical challenges to the cell design, although some problems were minimized during recent years.[3−5] Volume changes and the resulting disadvantages are generally less pronounced in the Li−Sn system, which is in the focus of the present study.

First investigations concerning the Li−Sn system date back to the beginning of the last century, when the existence of the three phases Li_4Sn, Li_3Sn_2, and Li_2Sn_5 was postulated[6] (cf. Figure 1). For Li_4Sn the possibility of an even higher lithium content in this phase was already noted, according to observations during crystallization. Indeed, the composition of this phase was subsequently revised to $Li_{22}Sn_5$ ($Li_{4.4}Sn$) based on crystal structure refinements,[7] though only temporarily, as should become clear later. Baroni[8,9] apparently also observed Li_2Sn_5, but gave the composition as $LiSn_4$. Shortly after, the presence of several intermetallic compounds in the binary phase diagram was proposed, namely, Li_4Sn, Li_7Sn_2, Li_5Sn_2, Li_2Sn, α-LiSn, and $LiSn_2$, highlighting the complexity of the Li−Sn system. Li_3Sn_2 and $LiSn_4$ were not observed during these studies.[10] In the 1970s Li_7Sn_2,[11] Li_5Sn_2,[12] and α-LiSn[13] were affirmed by crystal structure determinations, while the compositions Li_2Sn and $LiSn_2$ were corrected to Li_7Sn_3[14] and Li_2Sn_5,[15] respectively. In the following a new phase with a composition of $Li_{13}Sn_5$ was introduced,[16] and a second polymorph, β-LiSn, was obtained from a Ga-containing melt.[17] Thermodynamic studies aiming for the construction of an improved phase diagram indicated one more compound denoted as Li_8Sn_3, but this phase was not further characterized.[18]

In the beginning of this century, structure refinements based on single-crystal X-ray and powder neutron diffraction

Received: October 8, 2021
Published: April 13, 2022

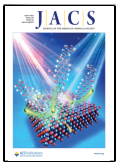

https://doi.org/10.1021/jacs.1c10640
J. Am. Chem. Soc. 2022, 144, 7096−7110

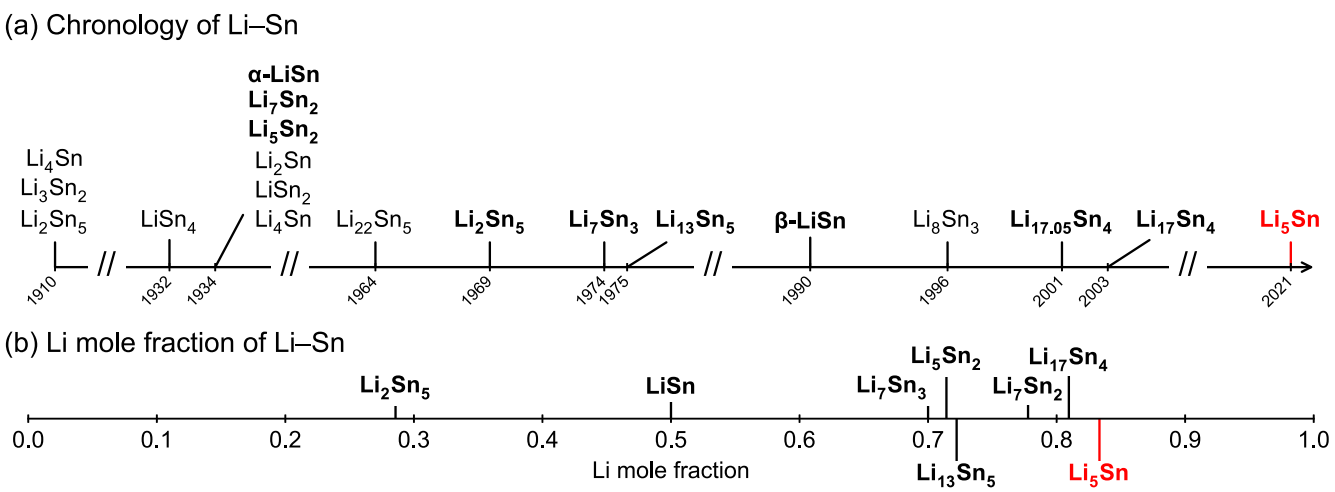

Figure 1. (a) Chronology of experimental reports of lithium stannides. Note that only the bold compositions are backed by structure determination and typically further investigations. For the other compositions no crystal structure data are available, composition assignments have been changed, or the presence of the phase has been completely refuted over time. (b) Li mole fractions of the experimentally confirmed lithium stannides.

demanded to once again reconsider the composition of $Li_{22}Sn_5$ ($Li_{4.4}Sn$). Specifically, the composition was refined to $Li_{17}Sn_4$ ($Li_{4.25}Sn$),[19,20] which, to the best of our knowledge, is the Li-richest binary stannide reported so far. This compound exhibits poor metallic behavior[20] and might be understood in a simple ionic picture according to $(Li^+)_{17}[Sn^{4-}]_4 \cdot e^-$ based on band structure and electron localization function calculations.[21] Difficulties in determining the composition and inconsistencies in occupations of crystallographic Li positions from different investigations might be related to a significant homogeneity range of this phase spanning from $Li_{17}Sn_4$ to $Li_{17.42}Sn_4$ (= "$Li_{21.8}Sn_5$").[22]

Figure 1a summarizes the Li−Sn chronology, and Figure 1b emphasizes the Li concentration of the verified phases. Phase diagrams including $Li_{17}Sn_4$, Li_7Sn_2, $Li_{13}Sn_5$, Li_5Sn_2, Li_7Sn_3, LiSn, Li_2Sn_5, and Li_8Sn_3 can be found in the literature.[18,23] Moreover, all known stable phases were recently studied with solid state NMR and Mössbauer spectroscopy to produce reference data for battery operando studies.[24]

Further metastable lithium-rich stannides with compositions of Li_5Sn and Li_7Sn were predicted based on *ab initio* calculations.[25,26] For Li_5Sn, two crystal structures were derived, both closely related in their local atomic surroundings, however, with differences in the arrangement and interconnection of the resulting coordination polyhedra.

In the present work, we describe the successful synthesis and structural characterization of Li_5Sn, which contains the already predicted coordination polyhedra, but again differently arranged. The thermodynamic stability of the obtained and various competing structures is investigated based on *ab initio* density functional theory (DFT) calculations, considering atomic vibrations, including anharmonicity, as well as electronic excitations at finite temperatures.

2. EXPERIMENTAL DETAILS

All manipulations were carried out in an Ar-filled glovebox (MBraun, Garching, Germany; $p(O_2)$ < 0.1 ppm, moisture and oxygen constantly removed by copper catalyst and molecular sieve), due to severe air and moisture sensitivity of lithium and the title compound. Synthesis was successful from tin powder (99.9%, Alfa Aesar) with an excess of lithium metal (rods, Merck) as flux and reaction medium with an overall Sn to Li molar ratio of 1:10 in a welded tantalum ampule (Aldrich). The tantalum ampule was heated in an Ar-filled fused silica tube at 100 K/h to 1073 K and directly allowed to cool to 673 K with a rate of 2 K/h, followed by natural cooling to room temperature. After thermal treatment, the sample mostly consists of $Li_{17}Sn_4$ and excess lithium. In order to remove the excess lithium, the opened Ta-ampule was transferred to an H-tube and washed several times with liquid ammonia until the liquid ammonia only showed a faint blue coloration, indicating just traces of elemental lithium being left in the sample (exposed to ammonia for about 1 h). During this operation $Li_{17}Sn_4$ decomposes to a so far unknown badly crystallized, tin-richer product, leaving crystals of Li_5Sn behind, which also decompose upon extended treatment of more than 1 day in liquid ammonia.

Single-crystal X-ray diffraction measurements were taken with a κ-CCD Bruker-Nonius single-crystal diffractometer (Mo Kα radiation, λ = 0.710 73 Å) and analyzed with the ShelX software package.[27] Further details on the crystal structure investigation may be obtained from the Fachinformationszentrum Karlsruhe, 76344 Eggenstein-Leopoldshafen, Germany (fax: (+49)7247-808-666; e-mail: crysdata@fiz-karlsruhe.de), on quoting the depository number CSD-2099217.

Chemical analysis on O, N, and H was carried out on a LECO ONH835 analyzer (LECO, St. Joseph, MI, USA), to confirm the composition.

3. COMPUTATIONAL METHODOLOGY

3.1. Structure Enumeration. Previously, new stable or metastable Li−Sn phases were explored by Mayo and Morris[26] using random structure searching[31,32] and by Sen and Johari[25] based on evolutionary crystal structure prediction,[33−35] both in combination with *ab initio* calculations. In these studies, Mayo and Morris[26] predicted hexagonal *P6/mmm* Li_5Sn, while Sen and Johari[25] predicted monoclinic *C2/m* Li_5Sn. In contrast, as detailed below in Section 4.1, the Li_5Sn structure observed in the present experiments obeys orthorhombic symmetry with the space group *Cmcm*. However, all three structures mentioned above consist of arrangements of Sn-centered capped hexagonal prisms surrounded by Li atoms as shown in Figure 2a. The difference among the structures lies only in the arrangement of the Sn coordination polyhedra perpendicular to the cap direction. Specifically, *P6/mmm* Li_5Sn consists exclusively of face-sharing Sn coordination polyhedra (Figure 2b). The Sn coordination polyhedra in *C2/m* and *Cmcm* Li_5Sn, in contrast, are both face- and edge-sharing (Figure 2c) but

https://doi.org/10.1021/jacs.1c10640
J. Am. Chem. Soc. 2022, 144, 7096−7110

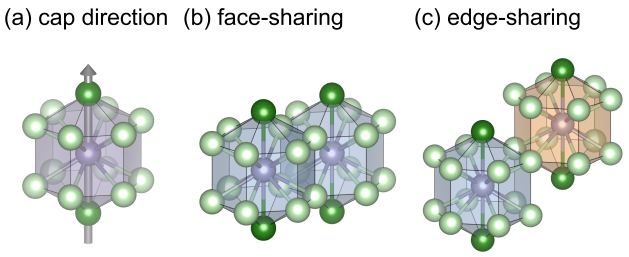

Figure 2. (a) Sn-centered bicapped hexagonal prism composed of 14 Li atoms. The cap direction is shown by the gray arrow. Gray spheres represent Sn atoms, and dark green and light green spheres represent Li atoms at the cap and the prism positions, respectively. (b) Two face-sharing Sn coordination polyhedra. (c) Two edge-sharing Sn coordination polyhedra. The polyhedra in the different colors are on different levels with respect to the cap direction (cf. Figure 3). Visualization was performed using VESTA.[28]

arranged in different ways. For the cap direction, every unit polyhedron shares the cap Li atoms with other polyhedra. As a consequence, all three Li_5Sn structures can be schematically understood in a two-dimensional configuration space as different arrangements of hexagons with two colors (Figure 3).

To investigate the thermodynamic stability of Li_5Sn in detail, we conducted *ab initio* simulations. Since various candidate crystal structures were already examined in the previous works of Mayo and Morris[26] and of Sen and Johari,[25] in the present study we intensively focused on the Li_5Sn structures consisting of the Sn coordination polyhedra described above. We however considered not only the above-mentioned three Li_5Sn structures but actually in total 108 arrangements of the Sn coordination polyhedra determined using the structure enumeration algorithm.[36,37] We considered up to eight hexagons in the unit cell in the two-dimensional configuration space. We mostly utilized the implementation in ICET (ver. 1.3),[38] but a few remarks are in order:

1. In the two-dimensional representation visualized in Figure 3, arrangements need to be omitted if they are equivalent to another arrangement via a color symmetry operation, i.e., by flipping the two colors. A corresponding symmetrization procedure was implemented by ourselves.
2. The cell shapes created according to point 1 are not immediately in the standardized representation. The latter is however beneficial to improve numerical stability of the DFT simulations. After enumeration, we therefore further conducted a two-dimensional Delaunay reduction.[29,30] Since the standardization implemented in ICET ver. 1.3 (Niggli reduction[30,39]) applies only to three-dimensional cases, we implemented a two-dimensional Delaunay reduction by ourselves.

In Figure 3 some of the thus obtained arrangements of Sn coordination polyhedra are described. They include the arrangements previously predicted by Mayo and Morris[26] (#0) and by Sen and Jonari[25] (#83). The arrangement found in the present experiments is #7 (cf. Section 4.1), while the arrangement showing the lowest energy at 0 K in the *ab initio* simulations is #23 (cf. Section 4.4). Structures #1 and #41 show the highest and the second lowest energies, respectively, at 0 K in the *ab initio* simulations.

Note that for some of the 108 structures, we could in principle make smaller primitive cells by choosing a lattice

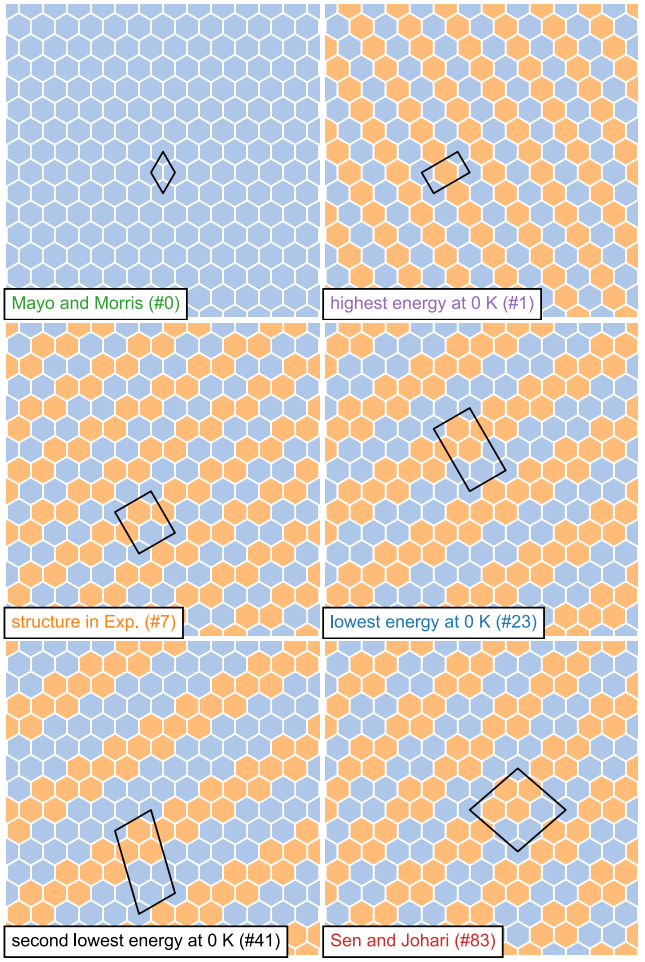

Figure 3. Two-dimensional schematics for some of the 108 arrangements of the Sn coordination polyhedra investigated in the present *ab initio* simulations. Each hexagon represents one Sn coordination polyhedron, a bicapped hexagonal prism consisting of 14 Li atoms. Hexagons of the same color (either blue or orange) indicate prisms lying on the same level and thus sharing their faces as shown in Figure 2b. Orange hexagons are shifted with respect to the blue ones along the direction perpendicular to the paper surface (i.e., along the cap direction) by half of the prism height. Thus, neighboring blue and orange hexagons represent edges sharing prisms as shown in Figure 2c. The parallelogram for each structure shows the projected unit cell standardized by the two-dimensional Delaunay reduction.[29,30]

basis that mixes the axial and the basal directions. However, as we have to determine very small energy differences (cf. Section 4.4), we prefer to keep computational consistency among all investigated structures as much as possible. Therefore, for all the 108 structures, we set one of the lattice vectors along the cap direction and chose the other two lattice vectors perpendicular to this cap-direction lattice vector. We further applied the same number of k points along the cap direction for all 108 structures.

3.2. Electronic Structure Calculations for the 108 Li_5Sn Structures. For all 108 Li_5Sn structures created systematically by structure enumeration (Section 3.1),[36,37] we conducted structure optimization. We employed the projector augmented wave (PAW) method[40] as implemented in VASP[41,42] in combination with the provided potentials.[43] The reciprocal space was sampled by the Methfessel−Paxton scheme[44] with a smearing width of 0.2 eV.

https://doi.org/10.1021/jacs.1c10640
J. Am. Chem. Soc. 2022, 144, 7096−7110

To make sure that our results are robust and insensitive with respect to the computational conditions, we tested five different computational settings summarized in Table 1.

Table 1. *Ab Initio* Computational Conditions Investigated in the Present Study[a]

	XC	cutoff (eV)	k space	valence	
				Li	Sn
A	PBE	200	≥16 128	2s	5s5p
B	PBE	500	≥16 128	2s	5s5p
C	PBE	200	≥21 600	2s	5s5p
D	PBE	500	≥16 128	1s2s	4d5s5p
E	LDA	200	≥16 128	2s	5s5p
F	PW91	200	≥16 128	2s	5s5p
G	SCAN	200	≥16 128	2s	5s5p

[a]The columns "XC", "cutoff", "k space", and "valence" refer to the exchange−correlation functional, the energy cutoff for the plane waves, the number of points per reciprocal atom sampled in the reciprocal space, and the orbitals treated as valence for each element, respectively. We also tested the energy cutoff of 700 eV (used by Sen and Johari[25]) and found negligible differences from 500 eV.

Specifically, we tested two cutoff energies (200 and 500 eV), two k-space mesh densities, and two sets of PAW potentials with different valence states. Further, in addition to the generalized gradient approximation (GGA) in the Perdew−Burke−Ernzerhof (PBE) form,[45] we also employed the local density approximation (LDA),[46,47] the GGA in the Perdew−Wang form (PW91),[48] and the strongly constrained and appropriately normed (SCAN) meta-GGA.[49,50] As detailed in Section 4.5, our conclusions are robust against these computational settings. Thus, we utilized setting A from Table 1 for further analysis of the 108 Li_5Sn structures.

Total energies were converged to within 1×10^{-5} eV per unit cell. Full structure relaxation was performed by optimizing cell volume, cell shape, and internal atomic positions so that the forces on atoms and the stress components on the unit cell are less than 1.5×10^{-3} eV/Å and 1×10^{-2} eV/Å^3, respectively.

To compare the phase stability of the 108 Li_5Sn structures with respect to the two-phase state of the known equilibrium phases, i.e., body-centered cubic (bcc) Li and $F\bar{4}3m$ $Li_{17}Sn_4$,[19,20] we also simulated these latter two phases with optimizing their structures. The same computational conditions (setting A from Table 1) and the same convergence criteria as above were applied. The energy difference of Li_5Sn referenced to the two-phase state was computed as

$$\Delta E = E(\mathrm{Li_5Sn}) - \left(\frac{1}{8}E(\mathrm{Li}) + \frac{7}{8}E(\mathrm{Li_{17}Sn_4})\right) \quad (1)$$

where $E(\alpha)$ denotes the energy of phase α per atom.

To get insight on the dependence of the phase stability of Li_5Sn on pressure and thermal expansion, we computed the energy−volume curves for the structures #0, #7, #23, and #83 at 13 fixed volumes within a range of 16−22 Å^3/atom. At each volume, both the cell shape and the internal atomic positions were optimized. For the stress components, both the diagonal terms (minus their mean values) and the off-diagonal terms were optimized to be less than 5×10^{-5} eV/Å^3. The structure optimization was repeated several times to be consistent with the given energy cutoff.

3.3. Cluster Expansion of the Sn Polyhedra Arrangement. To analyze the impact of the arrangement of the Sn coordination polyhedra on the energies of the 108 Li_5Sn structures, the cluster expansion (CE) method[51−53] was employed. While the CE method is typically applied to describe *atomic* configurations on a given 3D crystal lattice, in the present study we regard the Sn coordination polyhedra as the fundamental objects of the CE, which live on a 2D lattice. The two irreducible Sn coordination polyhedra along the Li cap direction that arise for the edge-sharing situation (Figure 2c) are mapped onto two types of elements (blue and orange) in the CE. They can be thought of as two distinct types of atomic species in a usual CE. These two elements can be arranged in different configurations via the CE on a two-dimensional triangular lattice. Note that due to symmetry, only the clusters involving even numbers of Sn coordination polyhedra like doublet and quartet clusters contribute to the energies, and there are no contributions of clusters with odd numbers of polyhedra like singlet and triplet clusters; in the schematics in Figure 3, this means that the color switching of *all* the polygons does not affect the energies. Note also that, unlike in typical CE applications, in the present study we consider a fixed atomic composition of Li_5Sn, with differences only in the arrangement of the Sn coordination polyhedra. The energy range for the effective cluster interactions (ECIs) and for the fitting error is therefore much smaller than in typical CE applications.

The ICET code[38] was utilized for the CE analysis. The ECIs for clusters with odd numbers of Sn coordination polyhedra were restricted to be zero. The ECIs were determined based on the least absolute shrinkage and selection operator (LASSO) regression.[54]

3.4. Gibbs Energies for Structures #7 and #23. The thermodynamic stability of Li_5Sn at finite temperatures was investigated for the two most relevant structures (Sn coordination polyhedra arrangements), i.e., the experimentally observed one (#7) and the energetically lowest one as determined from theory (#23).

To this end, we employed the thermodynamic integration using Langevin dynamics (TILD)[55,56] method, i.e., the combined application of thermodynamic integration,[57−59] free energy perturbation (FEP) theory,[57,60] and the Langevin thermostat.[61] Approaches based on the TILD concept can predict various material properties such as defect formation energies[55,62−64] and melting points[65,66] both accurately and efficiently.

We decomposed the Helmholtz energy $F(V, T)$ at temperature T and at volume V for a given structure as

$$F(V, T) = E^{\mathrm{DFT}}(V) + F_{\mathrm{vib,el}}(V, T) \quad (2)$$

where E^{DFT} is the conventional 0 K total energy of the system obtained by DFT calculations and $F_{\mathrm{vib,el}}$ the contribution of lattice vibrations and electronic excitations, including their adiabatic coupling. The contribution $F_{\mathrm{vib,el}}$ was obtained based on *ab initio* molecular dynamics (MD) in the finite-temperature DFT extension by Mermin,[67] where the Fermi−Dirac distribution at the corresponding temperature was applied to include the impact of electronic excitations. Note that the impact of the coupling between lattice vibrations and electronic excitations can be tens of meV/atom,[68] and its inclusion is therefore important for a high-accuracy prediction of the Helmholtz energy.

https://doi.org/10.1021/jacs.1c10640
J. Am. Chem. Soc. 2022, 144, 7096−7110

We computed $F_{vib,el}(V, T)$ as

$$F_{vib,el} = F_{vib,el}^{eh} + \Delta F_{vib,el}^{eh\rightarrow MTP} + \Delta F_{vib,el}^{MTP\rightarrow DFT} \quad (3)$$

The first term in eq 3 is the contribution of lattice vibrations to the Helmholtz energy, analytically computed based on an effective harmonic (eh) potential[69,70] (Appendix B.2 in the Supporting Information) obtained from *ab initio* MD results (Appendix B.1 in the Supporting Information). Using such a potential can provide a better approximation of the Helmholtz energy than the harmonic potential at 0 K[71] and therefore serve as a computationally better reference for the following thermodynamic integration.

The second term (eh → MTP) in eq 3 amounts to the difference between the Helmholtz energies of the system governed by the effective harmonic potential and that by a moment tensor potential (MTP),[72−75] and it is computed by thermodynamic integration. The MTP is a type of machine-learning interatomic potential that can predict accurate energies and atomic forces even for complex multicomponent systems[71,74,76] or systems with magnetic degrees of freedom.[77] In this work, the MTP was obtained by fitting to *ab initio* MD data (Appendix B.3 in the Supporting Information). Note that the accuracy of the MTP can be further systematically improved by using active learning techniques.[73−75,77−79]

The third term (MTP → DFT) in eq 3 is the difference between the Helmholtz energies of the system governed by the MTP and that by DFT and is computed by the first-order approximation of the FEP theory.[60] "Direct upsampling" was performed from MTP runs at each (V, T), wherein 10 random configurations were chosen and self-consistent DFT calculations were carried out to obtain the Helmholtz energy difference. The DFT Helmholtz energy was obtained based on the Fermi−Dirac distribution with the true electronic temperature in the formalism of Mermin;[67] that is, the contribution of electronic excitation to the Helmholtz energy was also considered here. The exchange−correlation functional, the plane-wave cutoff energy, the mesh for the reciprocal-space sampling, and the orbitals treated as valence states were the same as those chosen for the 0 K structure optimization (condition A in Table 1).

Each of the three terms in eq 3 was computed for seven volumes between 16 and 19 Å^3/atom and 12 temperatures from 50 K up to 600 K. The highest temperature of 600 K was set because, above 600 K, the MTP predicted a phase change at higher temperatures in structures #7 and #23 (Appendix E in the Supporting Information). These were then fitted to polynomials with the terms of T, TV, T^2, TV^2, and T^2V. The three terms in eq 3 were then summed up to provide the entire Helmholtz energy surface $F(V, T)$ for a dense grid of temperatures and volumes. Then, the Gibbs energy $G(p, T)$, where p is the pressure, was computed via a Legendre transformation, which is shown in Section 4.8.

4. RESULTS AND DISCUSSION

4.1. Experimental Section. Li_5Sn was obtained as described in Section 2 in the form of gray crystals with no recognizable shape and sizes of around 0.3 mm. The excess lithium together with tin probably provides a melt functioning as self-flux for enhanced crystal growth of the Li-rich compounds.[80] Li_5Sn forms as a byproduct of $Li_{17}Sn_4$. During treatment with liquid ammonia $Li_{17}Sn_4$ is apparently decomposed in a reaction with ammonia to a badly crystallized Li-poor product, indicating the redox activity of ammonia. This was earlier observed in similar reactions of intermetallic phases, for example, the oxidation of silicide or germanide Zintl ions to new tetrel element modifications[81−83] or to framework clathrate structures by protic reactants as organic ammonium ions, HCl, or water,[84] to name only few. The Li_5Sn crystals are more kinetically stable against attack of ammonia and thus can be isolated after brief exposure. However, upon extended contact to liquid ammonia, these crystals also degrade. The crystal structure contains mutually isolated tin atoms entirely surrounded by lithium atoms, putting forward an interpretation of Sn^{4-} in a metallic Li matrix, in other words $(Li^+)_5[Sn^{4-}]\cdot e^-$, as similarly discussed for $Li_{17}Sn_4$.[21] The results of the crystal structure refinements leave little room for unnoticed deviations from the derived composition. In order to exclude the presence of unintended contamination by hydrogen or small amounts of oxygen or nitrogen, a chemical analysis on these elements by the hot gas extraction technique was carried out, resulting in only negligible concentrations calculated to an overall composition of $Li_5SnN_{0.0005}O_{0.13}H_{0.06}$. The small oxygen contamination is typical for a highly air- and moisture-sensitive compound and likely to originate in a brief air contact during transfer of the only mechanically closed tin capsules from the glovebox to the analyzer.

Table 2 shows the lattice parameters and the fractional atomic coordinates of Li_5Sn obtained from experiments.

Table 2. Lattice Parameters and Fractional Atomic Coordinates of Li_5Sn in *Cmcm* (#7) from Experimental Structure Determination at Room Temperature in Comparison with Those Obtained from *Ab Initio* Calculations[a]

		experimental	*ab initio*
compound		Li_5Sn	
crystal system		orthorhombic	
space group		*Cmcm* (no. 63)	
number of formula units Z		4	
a (Å)		5.6638(4)	5.701
b (Å)		9.3417(8)	9.108
c (Å)		8.0477(6)	8.206
volume V (Å^3)		425.80(6)	426.06
density ρ_{calc} (g cm^{-3})		2.393	2.392
Li(1) 4*c*	*x*	0	0
	y	0.3984(12)	0.384 96
	z	1/4	1/4
Li(2) 16*h*	*x*	0.2492(8)	0.241 70
	y	0.1193(5)	0.125 40
	z	0.0756(7)	0.082 41
Sn 4*c*	*x*	1/2	1/2
	y	0.35493(3)	0.368 24
	z	1/4	1/4

[a]Details of the structure refinement are found in Table 3.

Details of the structure refinement are found in Table 3. Li_5Sn crystallizes in the orthorhombic space group *Cmcm* with only one crystallographic site for Sn and two for Li. Sn and Li(1) with equal multiplicity (Wyckoff site 4*c*) are situated in hexagonal prisms of Li(2) with four times larger multiplicity (site 16*h*). These hexagonal prisms around Sn are capped by two Li(1) and *vice versa* to yield 14-fold coordinations. The 11-fold coordination of Li(2) atoms resembles an Edshammar polyhedron, which occurs rather frequently in intermetallic

https://doi.org/10.1021/jacs.1c10640
J. Am. Chem. Soc. 2022, 144, 7096−7110

Table 3. Selected Parameters in Experimental Structure Determination of Li_5Sn in *Cmcm* (#7) in Experiments

temperature T (K)	293
diffractometer	κ-CCD Bruker-Nonius
wavelength λ (Å)	0.710 73
monochromator	graphite
$2\theta_{max}$ (deg)	54.90
absorption coefficient μ (mm^{-1})	5.750
h, k, l	$-7 \le h \le 5$
	$-12 \le k \le 12$
	$-10 \le l \le 10$
measured reflections	3979
unique reflections	291
R_{int}, R_σ	0.0476, 0.0177
refined parameters	19
goodness-of-fit on F^2 (GoF)	1.181
R_1, wR_2	0.0154, 0.0384
extinction parameter	0.0030(8)
$F(000)$	260
largest peak, deepest hole in e^- difference map ($Å^{-3}$)	0.84, −0.36

compounds.[85,86] All three occurring coordination polyhedra are depicted in Figure 4. These are markedly different from

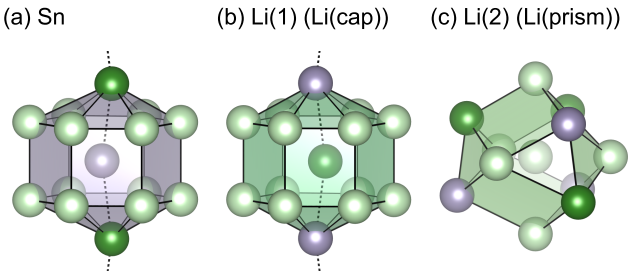

Figure 4. Coordination polyhedra around (a) Sn, (b) Li(1), and (c) Li(2) occurring in the experimentally observed Li_5Sn structure with the space group *Cmcm* (#7 in Figure 6). Gray, dark green, and light green spheres represent Sn, Li(1), and Li(2), respectively. Note that the alternative notations Li(cap) and Li(prism) are from the viewpoint of the Sn coordination polyhedra and are used for the *ab initio* analysis in Section 4.7.

those occurring in $Li_{17}Sn_4$, which, as most previously characterized binary Li-rich stannides, can be structurally related to an ordered body-centered cubic packing of Li and Sn, distorted by the different spatial requirements of both metals.[16] Tables 4 and 5 show the interatomic distances and angles, respectively, of Li_5Sn obtained from experiments. The Sn−Li distances of 2.8609(16) Å for Li(1) and 2.972(5)−3.172(5) Å for Li(2) are in the expected range as compared to those obtained for $Li_{17}Sn_4$ with similar high coordination numbers and probably the same electronic situation.[19] The shortest distance Sn−Li(1) is located in voids of a hexagonal channel of Li(2). In order to maximize this distance, both Sn and Li(1) are slightly displaced from the center of the coordination polyhedron parallel to [010] in opposite directions, resulting in the Li(1)−Sn−Li(1) angle of 163.7(4)° as depicted in Figure 4.

Figure 5a shows a section of the experimental crystal structure of Li_5Sn emphasizing the framework of vertex-, edge-, and face-sharing bicapped hexagonal prisms around Sn. In this structure, the polyhedra around Sn share the opposite capping

Table 4. Interatomic Distances of Li_5Sn in *Cmcm* (#7)[a]

		distance (Å)	
	quantity	experimental	*ab initio*
Sn−Li(1)	2	2.8609(16)	2.854
Sn−Li(2)	4	2.972(5)	2.992
	4	2.986(5)	3.056
	4	3.172(5)	3.046
Li(1)−Li(2)	4	2.871(9)	2.976
	4	2.986(5)	3.101
	4	3.280(10)	3.062
Li(2)−Li(2)	1	2.539(9)	2.655
	1	2.729(9)	2.644
	1	2.806(11)	2.750
	1	2.822(10)	2.756
	1	2.841(10)	2.945

[a]Quantities are evaluated with focusing on the first atom.

Table 5. Interatomic Angles of Li_5Sn in *Cmcm* (#7)[a]

		angle (deg)	
	quantity	experimental	*ab initio*
Sn−Li(1)−Sn	1	163.7(4)	173.9
Li(1)−Sn−Li(1)	1	163.7(4)	173.9
Li(1)−Sn−Li(2)	2	56.6(2)	60.5
	2	61.36(10)	63.2
	2	68.4(2)	63.1
	2	109.3(2)	114.3
	2	117.15(10)	116.7
	2	125.3(2)	122.1

[a]Quantities are evaluated with focusing on the pair of first and second atoms. The angles of Sn−Li(1)−Sn and Li(1)−Sn−Li(1) are symmetrically equivalent.

Li(1) vertices parallel to [100]. For polyhedra around Li(1) this applies correspondingly, sharing opposite capping vertices of Sn, resulting in parallel slightly kinked chains of alternating Sn and Li(1) atoms within this direction located in a hexagonal primitive channel of Li(2). The coordination polyhedra around Sn are connected to eight other Sn coordination polyhedra in the edge-sharing manner and to four further ones via rectangular face-sharing within (100). This face-sharing leads to zigzag chains parallel to [001].

4.2. Structural Comparison between Experiment and *Ab Initio* for *Cmcm* Li_5Sn. In Table 2, the structural parameters of *Cmcm* Li_5Sn (structure #7 in the enumeration) obtained from the *ab initio* calculations at 0 K are compared with those obtained from our experiments. The differences in the lattice parameters lie in the range of 1% to 2%, which is a typical range of deviation for the standard exchange−correlation functionals (e.g., refs 87 and 88). Thus, the comparison of the geometry of the specific *Cmcm* Li_5Sn structure provides a reasonable agreement with experiment in terms of structural data.

4.3. Structural Characteristics of the Li_5Sn Family. The *Cmcm* structure observed in the experiments is different from the structures previously reported in *ab initio* investigations on Li_5Sn.[25,26] However, as described in Section 3.1, the experimental and the previous *ab initio* structures can be understood as different arrangements of the bicapped hexagonal prisms with Sn at the center and with a frame of 14 Li atoms, among which 2 and 12 are on the cap and the prism positions, respectively (cf. Figure 4a). Indeed, there exists a

https://doi.org/10.1021/jacs.1c10640
J. Am. Chem. Soc. 2022, 144, 7096−7110

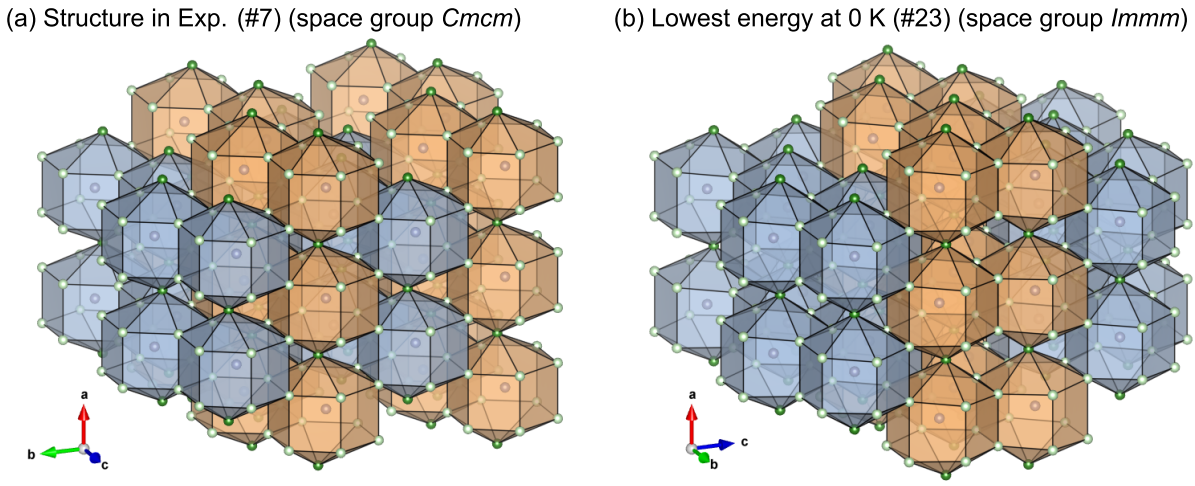

Figure 5. (a) Li_5Sn with the space group *Cmcm* found in the present experiments. (b) Li_5Sn with the space group *Immm* showing the lowest energy at 0 K in the *ab initio* simulations. Li(1) (Li(cap)) atoms are shown in dark green, Li(2) (Li(prism)) atoms in light green, and Sn atoms in gray. Sn coordination polyhedra in different colors (blue and orange) are connected in an edge-sharing manner (cf. Figure 3).

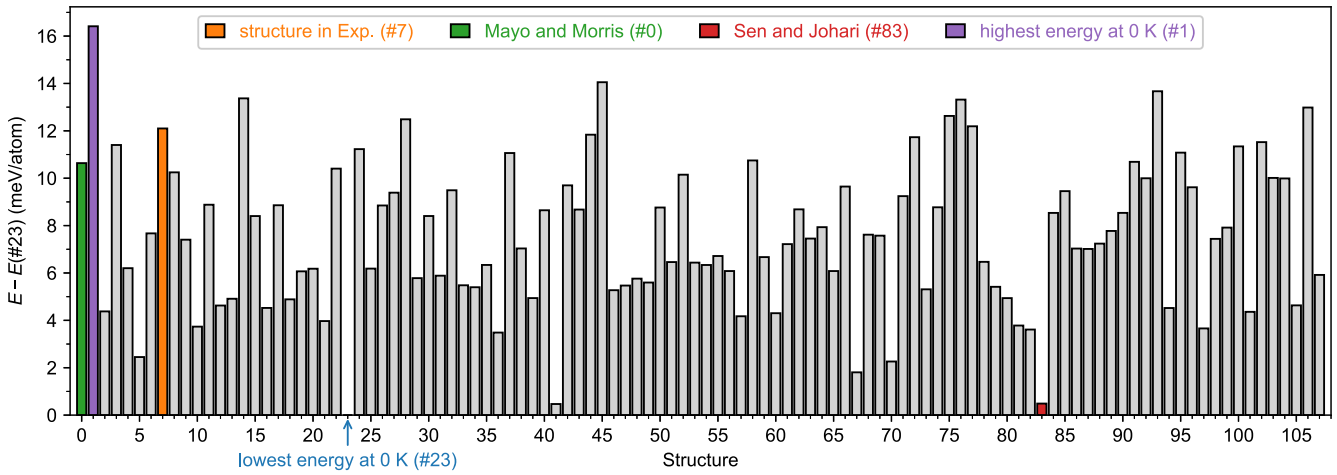

Figure 6. Comparison of *ab initio* computed energies of the 108 Li_5Sn structures at 0 K at their optimized atomic positions. The energy of structure #23, which shows the lowest value, is set as the reference.

large family of such structures that feature the capped hexagonal prisms as the basic entity which can be systematically arranged by the technique of structure enumeration (cf. Section 3.1). The Li coordination polyhedra are also similar among all of these structures; the coordination polyhedra around Li(cap) are always bicapped hexagonal prisms consisting of two Sn and 12 Li(prism) atoms, like in Figure 4b, and the coordination polyhedra around Li(prism) Edshammer polyhedra[85,86] consisting of three Li(cap), five Li(prism), and three Sn atoms like in Figure 4c, where only the arrangements of Sn and Li differ among the structures. In order to provide a comprehensive phase stability analysis, we thus consider a large subset of Li_5Sn structures from this family (specifically 108 structures) with different arrangements of the polyhedra generated by structure enumeration.

4.4. Phase Stability at 0 K. Figure 6 shows the *ab initio* computed energies of the 108 Li_5Sn structures at 0 K with relaxed atomic positions and relaxed cell shape. Structure #23 is found to be energetically the most stable one among all the structures. Structure #23 has a space group of *Immm* (No. 71) and is different from those found in the previous *ab initio* investigations, i.e., from the one found by Mayo and Morris (#0, *P6/mmm* (No. 191), +10.6 meV/atom)[26] and by Sen and Johari (#83, *C2/m* (No. 12), +0.5 meV/atom).[25] Structure #23 is also distinct from the experimental structure (*Cmcm* (No. 63)), which in Figure 6 corresponds to #7. At 0 K, the experimental Li_5Sn structure (#7) is higher in energy by +12.1 meV/atom than the computationally determined lowest-energy structure (#23). Figure 5b shows the arrangement of the Sn coordination polyhedra in structure #23. The lattice parameters of structure #23 are a = 5.763 Å, b = 8.156 Å, and c = 13.681 Å, and the fractional atomic coordinates are summarized in Table 6.

One may notice that the energy differences among the three lowest-energy structures (#23, #41, #83) vary only within 0.5 meV/atom. As detailed in Section 4.5, however, these energy differences are very robust against detailed computational conditions, and thus we can conclude with confidence that in DFT at 0 K the structure #23 is the energetically most stable phase with the composition of Li_5Sn.

Figure 7 shows the computed energy−volume curves at 0 K for some of the structures. Structure #23 is found to be

https://doi.org/10.1021/jacs.1c10640
J. Am. Chem. Soc. 2022, 144, 7096−7110

Table 6. Fractional Atomic Coordinates for Structure #23 with the Space Group *Immm* As Obtained in the *Ab Initio* Simulations with Setting A in Table 1

	Wyckoff	*x*	*y*	*z*
Li	16*o*	0.761 46	0.331 46	0.164 01
Li	8*n*	0.224 98	0.162 46	0
Li	4*j*	1/2	0	0.844 39
Li	2*c*	1/2	1/2	0
Sn	4*i*	1/2	1/2	0.319 55
Sn	2*d*	0	1/2	0

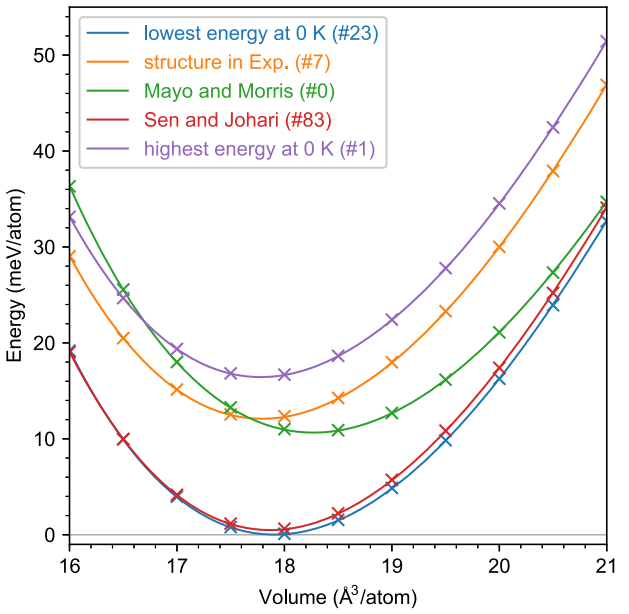

Figure 7. *Ab initio* computed energy−volume relations of Li_5Sn at 0 K. The curves are obtained by fitting the energy−volume relations to the Vinet equation of state.[89,90] The minimum energy of the structure #23 is set as the reference.

energetically the most stable one for most of the investigated volumes, and structure #7, found in the present experiments, is substantially higher in energy than structure #23. This implies that, by the application of pressure, it is *unlikely* that the experimentally observed structure #7 could be thermodynamically stabilized over structure #23.

The just presented phase-stability analysis among the 108 Li_5Sn structures reflects only the energetic competition at a fixed composition of $83.\overline{3}$ at. % Li. To investigate whether phase decomposition into a two-phase state is energetically more favorable than the best Li_5Sn structure (i.e., #23), specifically a decomposition into the end-member phase bcc Li and the known stable phase $F\overline{4}3m$ $Li_{17}Sn_4$, we have invoked eq 1. Indeed, we find that structure #23 of Li_5Sn is 9.8 meV/atom higher in energy than the two-phase state, which means that structure #23 (as well as any of the other investigated Li_5Sn structures) does not correspond to an equilibrium state but to a thermodynamically metastable phase at 0 K and under zero pressure.

4.5. Robustness against Computational Conditions. To make sure that our results are robust and insensitive to the details of the computations despite the small energetic differences, we tested various computational settings, including different cutoff energies, different *k*-space mesh densities, PAW potentials with different valence states, and various exchange−correlation functionals (cf. Section 3.2 and specifically Table 1). Figure 8 shows the resulting energy comparison among these computational settings in the form of correlation plots, with the energy of structure #23 set as the reference. For all investigated computational settings, structure #23 is clearly found to be the energetically lowest one among the 108 Li_5Sn structures. In fact, all the energy differences among the 108 structures are very similar among the various computational settings, as evidenced by the crosses lying closely to the diagonal in the correlation plots. For the PBE calculations (Figure 8a−c), we see a nearly perfect correlation, and even between different exchange−correlation functionals we see a good correlation (Figure 8d−f). These results substantially strengthen our confidence in that the phase stability among the 108 investigated Li_5Sn structures as obtained in the *ab initio* calculations is reliable and that structure #23 can be conclusively regarded as the energetically most stable one among the 108 structures at 0 K on the DFT level.

4.6. Impact of the Arrangement of the Sn Coordination Polyhedra on Phase Stability. To understand how the arrangement of the Sn coordination polyhedra is related to the relative energies of the Li_5Sn structures, we employ the CE method (Section 3.3). Figure 9a shows the ECIs obtained when the doublet and the quartet clusters, i.e., clusters made of two and four Sn coordination polyhedra, are considered in the expansion. The largest contribution to the energy comes from the first three smallest doublet clusters, which are visualized in Figure 9b. The absolute values of their ECIs decrease with the increase of the maximum projected distance D between the centers of the Sn coordination polyhedra within the clusters. Further, a quartet cluster, which is also visualized in Figure 9b, has an ECI whose absolute value is larger than 1 meV/atom. This highlights the importance of this quartet cluster to be included for an accurate energy prediction. In particular, the quartet cluster is more important than the doublet cluster with the projected distance $\sqrt{7}D \approx 2.646D$ between the centers of the Sn coordination polyhedra.

As found from Figure 9a, the first-nearest neighbor doublet cluster shows a negative ECI, which means that the Sn coordination polyhedra favor being connected with each other in the face-sharing manner. It is, however, critical to realize that there is a counteracting contribution from the second- and the third-nearest neighbor doublet clusters as well as the above-mentioned quartet cluster, which can stabilize Li_5Sn structures involving edge-sharing Sn coordination polyhedra in rather sophisticated ways. In particular, the two doublet clusters with positive ECIs favor configurations where the second and third nearest-neighbor coordination polyhedra are shifted against each other by one-half along the cap direction (i.e., they favor orange-blue occupations).

We can quantify the importance of the various clusters by the analysis of the root-mean-square error (RMSE) of the energies predicted by the CEs including specific clusters, as summarized in Table 7. In the extreme limit, when only the first nearest-neighbor doublet cluster is included, we obtain an RMSE of 2.702 meV/atom, which is large compared to the relevant energy scale (≈16 meV/atom, cf. Figure 6). When four doublet but no quartet clusters are included, the RMSE reduces to 1.300 meV/atom. This value is still appreciable due to the comparably small overall energetics. This statement is better supported by the scatter observed in the correlation plot in Figure 10a for the CE containing only doublet clusters. Even

https://doi.org/10.1021/jacs.1c10640
J. Am. Chem. Soc. 2022, 144, 7096−7110

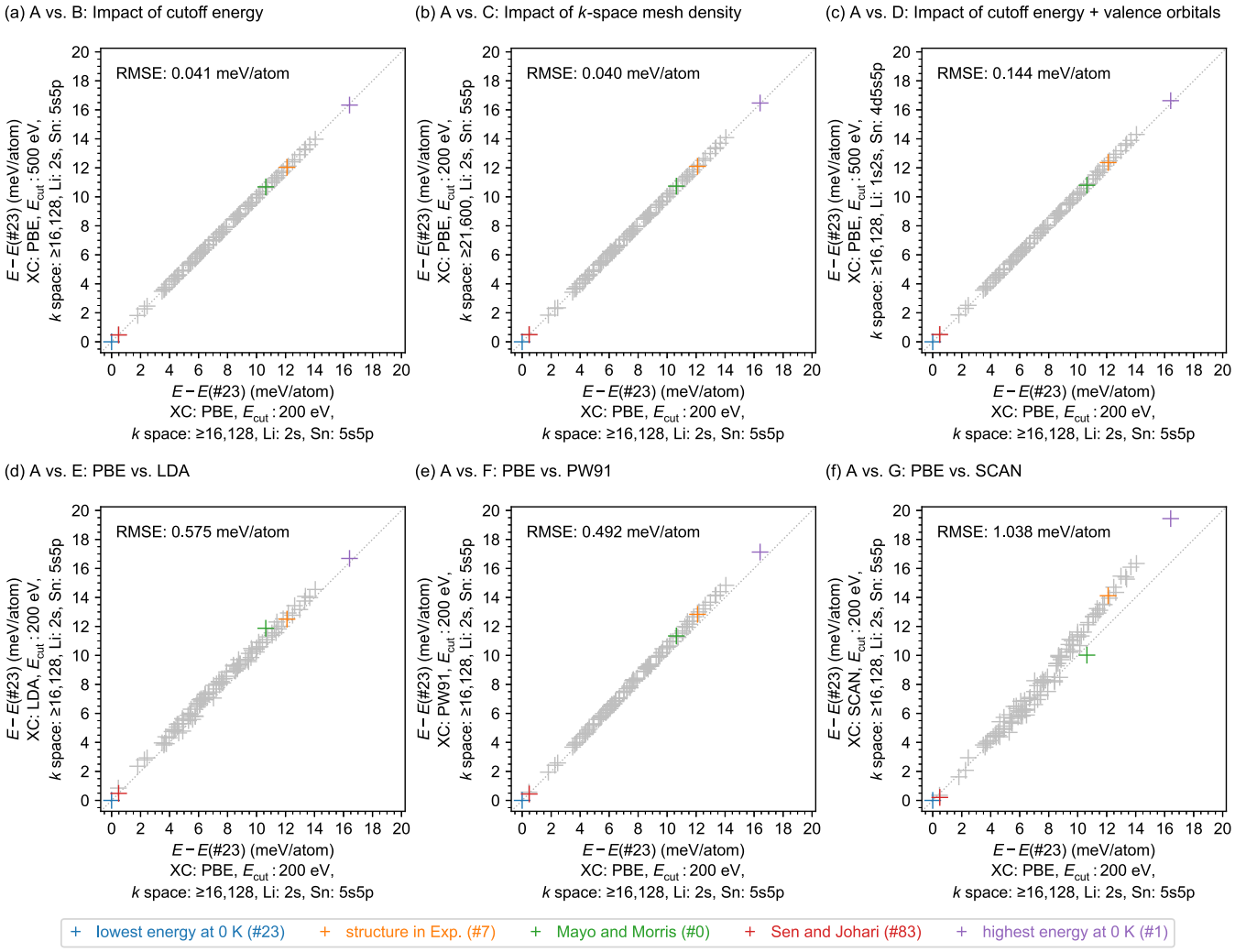

Figure 8. Comparison among the various computational settings listed in Table 1 for the *ab initio* computed energies at 0 K of the 108 investigated Li_5Sn structures. The energy of structure #23 is set as the reference.

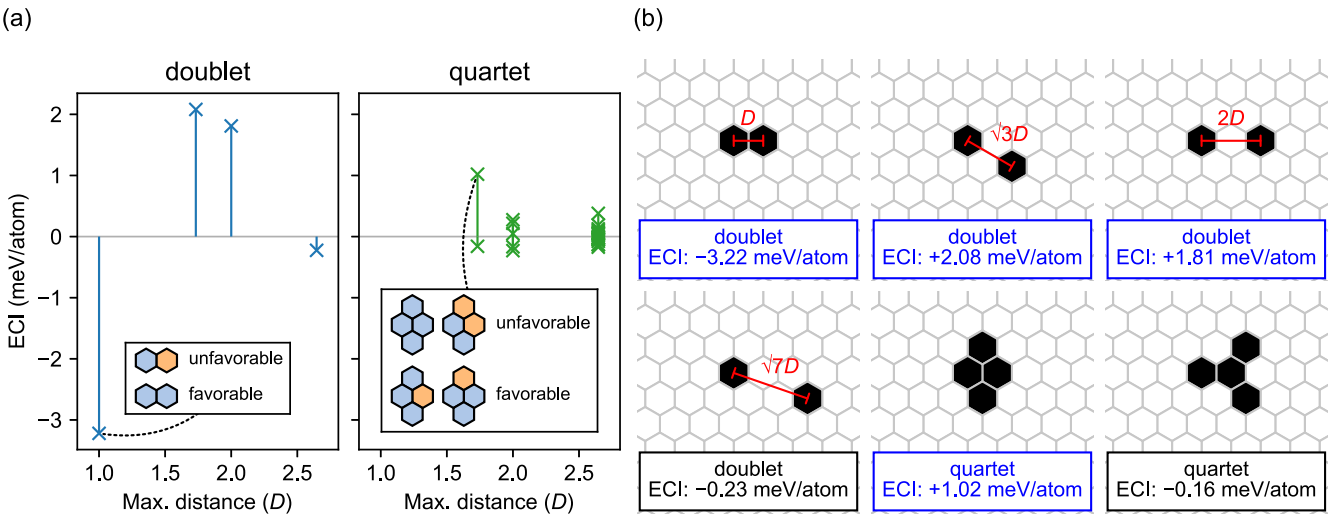

Figure 9. (a) ECIs obtained from the CE considering four doublet and 25 quartet clusters. The unit of the horizontal axis is the projected distance between the nearest-neighbor Sn coordination polyhedra *D*. Some typical arrangements of the polyhedra in the specified clusters and how they contribute to the energy are shown in the boxes. (b) Smallest doublet and quartet clusters. The clusters annotated by blue text show the largest absolute values of ECIs.

https://doi.org/10.1021/jacs.1c10640
J. Am. Chem. Soc. 2022, 144, 7096−7110

Table 7. Dependence of the RMSE of the Energies Predicted by the CE Method on the Numbers of Doublet and the Quartet Clusters Included in the Expansion[a]

doublet	quartet	RMSE (meV/atom)
1	0	2.702
2	0	2.349
2	1	1.832
2	2	1.776
3	0	1.415
3	1	0.818
3	2	0.810
3	7	0.727
4	0	1.300
4	1	0.741
4	2	0.738
4	7	0.616
4	25	0.388

[a]Starting in the first row of the table with an expansion containing only the strongest first nearest-neighbor doublet cluster (cf. doublet cluster with 1*D* in Figure 9b), the following rows represent expansions with successively more doublet and quartet clusters. For the rows with the same number of doublet clusters, quartet clusters with successively larger distances $D_{quartet}$ are included, but only up to a $D_{quartet} \leq D_{doublet}$, where $D_{doublet}$ is the maximum distance of the included doublet cluster.

worse, such a CE fails to correctly predict the lowest-energy structure (#23).

In contrast, when we add the above-discussed quartet cluster with an ECI of +1.02 meV/atom (cf. Figure 9b) instead of the fourth doublet cluster, the RMSE reduces down to 0.818 meV/atom, which confirms the importance of this quartet cluster. When the whole set of doublet and quartet clusters is considered, the correlation is further significantly improved, as indicated by the RMSE reducing down to 0.388 meV/atom. In fact, it is essential to include the quartet clusters for correctly predicting the lowest-energy structure #23, as demonstrated in Figure 10b.

4.7. Sn−Li Distances and Their Relation to Energies.

Figure 11 displays the average distances from Sn to two types of Li, i.e., Li(prism) and Li(cap), for all of the 108 Li_5Sn structures. As emphasized by the large gap between the two gray-shaded regions, the average Sn−Li(prism) distance is substantially larger than the Sn−Li(cap) distance for all structures. This finding is nicely consistent with the observed interatomic distances in the experimentally found *Cmcm* Li_5Sn structure (#7) (cf. Table 4). Indeed, we see a good quantitative agreement between the theoretical prediction (orange dots in Figure 11) and experiment (orange crosses) for structure #7.

Figure 12 shows various correlation plots among the relevant energetic and geometric quantities for the 108 Li_5Sn structures. Between the average Sn−Li(cap) distance and the relative energies (Figure 12a), there is a strong anticorrelation with a Pearson coefficient of −0.942, which implies that longer Sn−Li(cap) distances are energetically preferable. In relation with the CE discussion in Section 4.6, we can state that the structures lower in energy profit from an easier elongation of the Sn−Li(cap) distance. The elongation of the Sn−Li(cap) distance is mostly achieved by the elongation of the lattice parameter along the cap direction, as demonstrated by the strong positive correlation between them (Figure 12d). Further, the off-centering of Sn in its coordination polyhedron also contributes to an increase of the Sn−Li(cap) distance, as found from the positive correlation between the Li(cap)−Sn−Li(cap) angle and Sn−Li(cap) distance (Figure 12e).

There is also a positive correlation between the average Sn−Li(prism) distance and the relative energies (Figure 12b) with a Pearson coefficient of +0.698, which is however not as strong

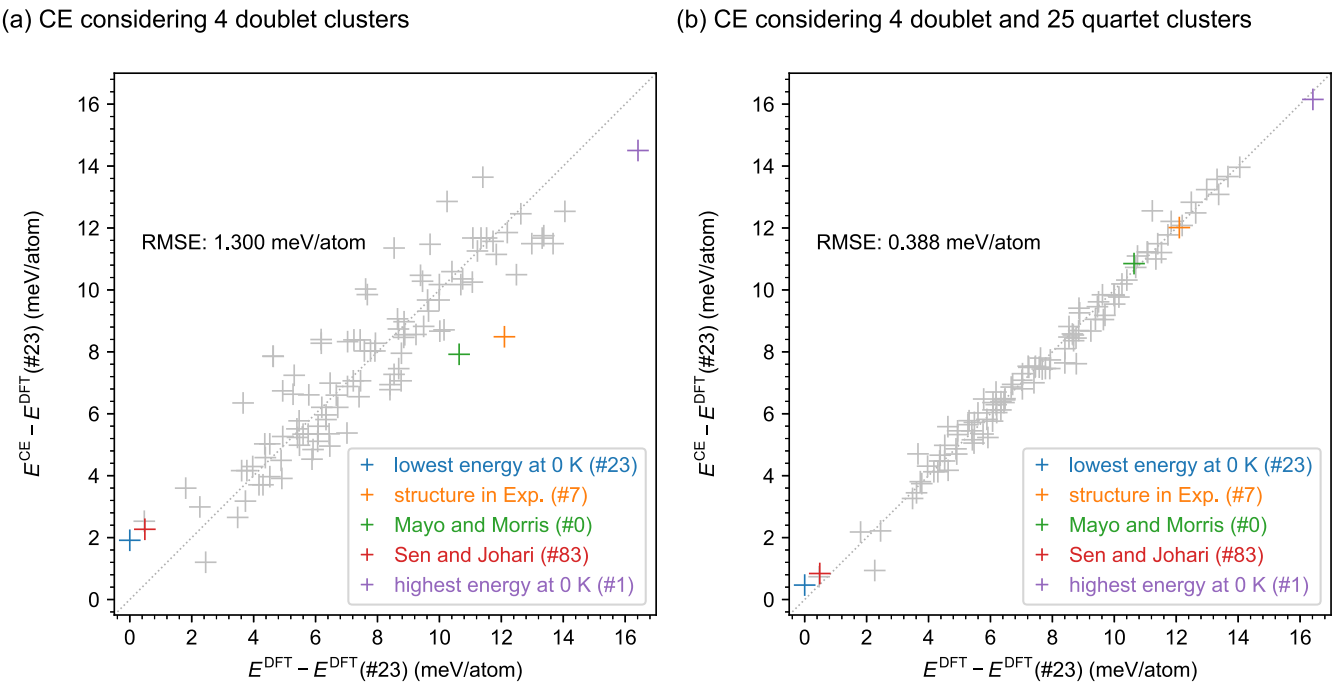

Figure 10. Comparison of *ab initio* computed energies at 0 K for the 108 Li_5Sn structures with those obtained from the CE method. The energy of structure #23 obtained from the *ab initio* calculation is set as the reference. (a) CE considering only the doublet clusters for the fitting. (b) CE considered both the doublet and the quartet clusters for the fitting.

https://doi.org/10.1021/jacs.1c10640
J. Am. Chem. Soc. 2022, 144, 7096−7110

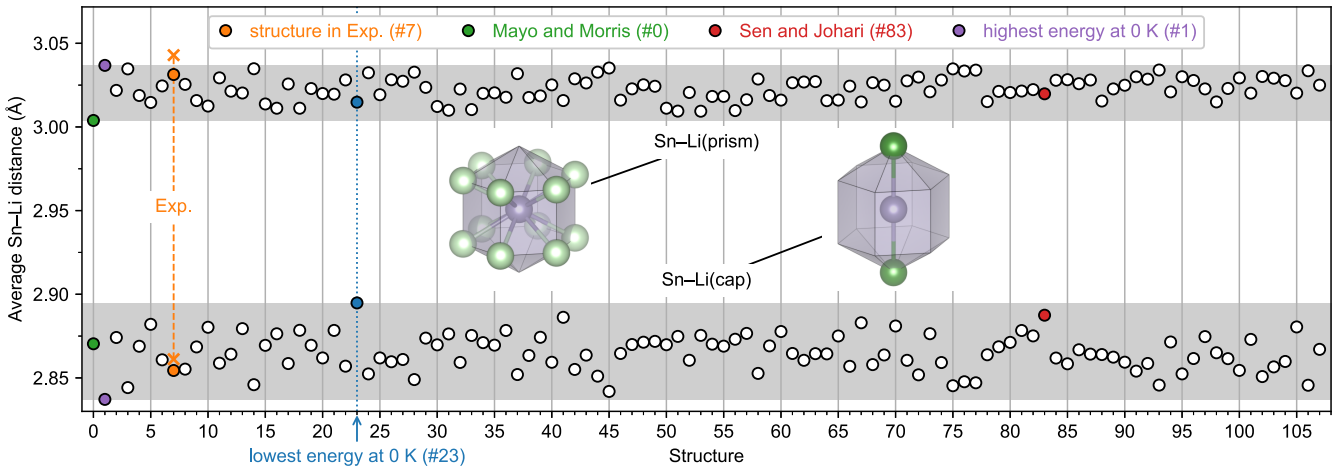

Figure 11. Comparison of the average Sn−Li distances for the 108 Li_5Sn structures at 0 K at their optimized atomic positions. The crosses for structure #7 indicate the values observed in our experiments at ambient temperature.

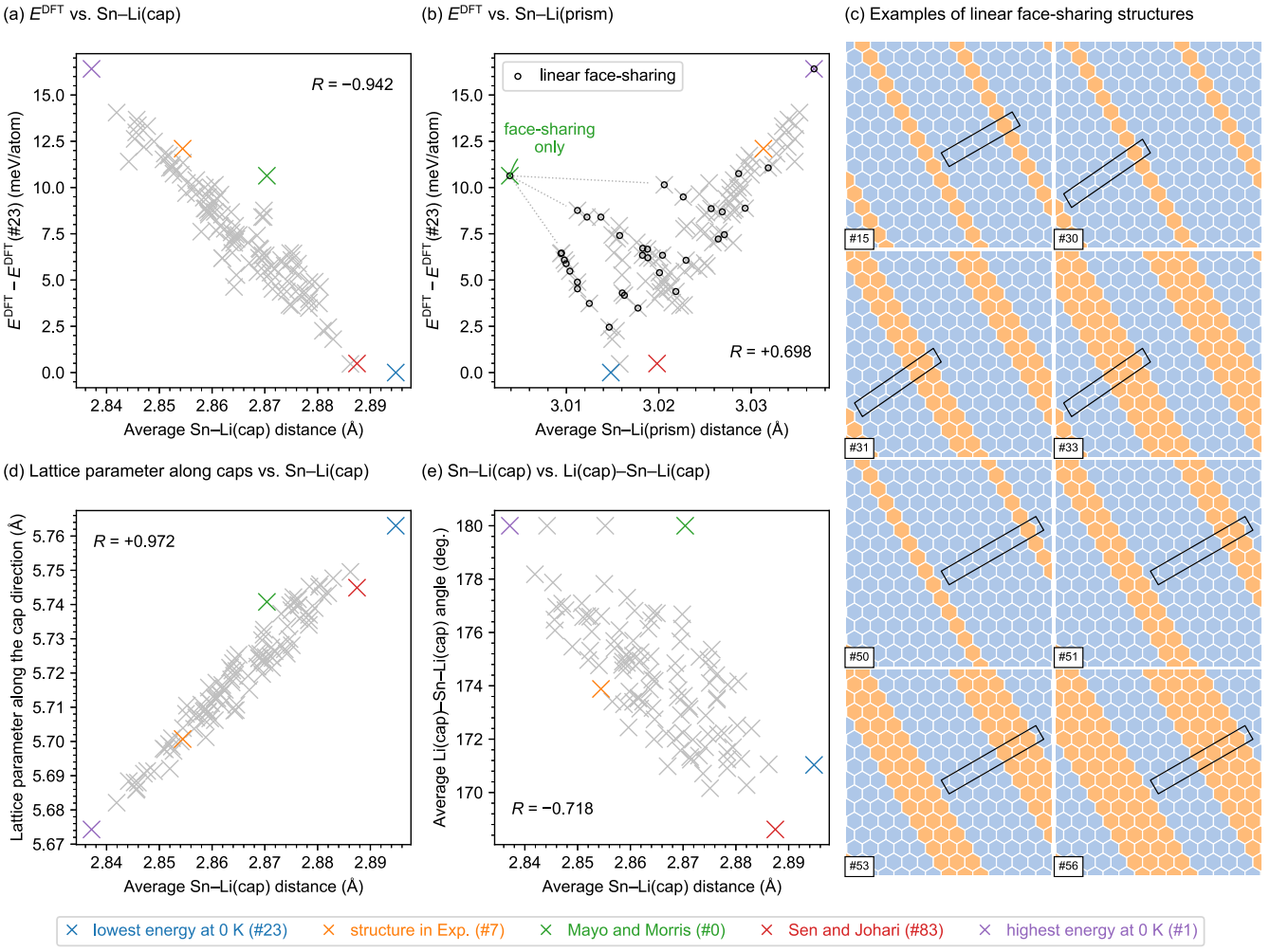

Figure 12. (a, b) Correlations of the *ab initio* computed energies at 0 K with (a) the average Sn−Li(cap) distances and (b) the average Sn−Li(prism) distances for the 108 Li_5Sn structures. Dashed gray lines are guides for the eyes. (c) Examples of linear face-sharing arrangement of Sn coordination polyhedra in the same representation style as Figure 3. (d) Correlation between the lattice parameters along the cap direction and the average Sn−Li(cap) distances. (e) Correlation between the average Li(cap)−Sn−Li(cap) angles and the average Sn−Li(cap) distances.

as the anticorrelation between the average Sn−Li(cap) distance and the relative energies (Figure 12a). The correlation is primarily broken by a few streaks of data points (dashed gray lines in Figure 12b), which can be identified with structures involving linear ordering of face-sharing Sn coordination polyhedra, as exemplified in Figure 12c. This implies a relation between the Sn−Li(prism) distance and the type of connection between the Sn coordination polyhedra. Figure

https://doi.org/10.1021/jacs.1c10640
J. Am. Chem. Soc. 2022, 144, 7096−7110

13 shows the corresponding correlation plot between the average Sn−Li(prism) distance and the average correlation

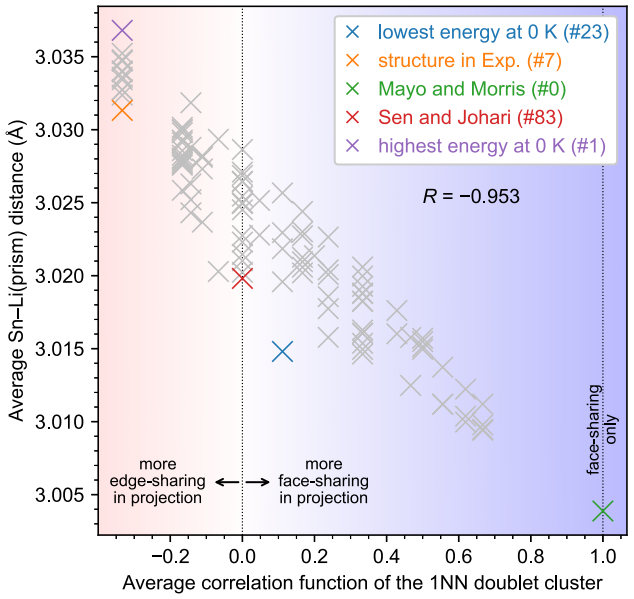

Figure 13. Correlation of the Sn−Li(prism) distances and the average correlation functions of the 1NN doublet clusters for the 108 Li_5Sn structures.

function of the first nearest-neighbor (1NN) doublet clusters, which accounts for the number of face- and edge-sharing polyhedra in the structure. There is a strong anticorrelation between these properties, as indicated by the Pearson coefficient of −0.953. That is, the more the 1NN polyhedra are arranged in a face-sharing manner, the shorter the Sn−Li(prism) distances are. As found in Section 4.6, however, it is essential for an accurate energy prediction to take the doublet clusters beyond the 1NN as well as the quartet clusters into account.

4.8. Phase Stability for Li_5Sn at Finite Temperatures.

Based on the detailed analysis in foregoing subsections, we can confidently claim that, at 0 K and at the composition of Li_5Sn, *ab initio* predicts structure #23 with the space group of *Immm* as the lowest-energy structure. Since this structure is different from the experimentally found one (#7), the experimental *Cmcm* Li_5Sn phase is metastable and may therefore be realized either by (1) thermodynamic stabilization at finite temperature or (2) due to kinetic reasons during the experimental process. To check the first possibility, i.e., whether the experimental structure #7 could be stabilized at finite temperatures due to lattice vibrations or electronic excitations, we further computed the Gibbs energy at finite temperature based on *ab initio* calculations. Specifically, we utilized the TILD approach[55,56] with an intermediate MTP potential to get accurate Gibbs energies at finite temperatures (Section 3.4) with considering both lattice vibrations, including full anharmonicity, and electronic excitations.

Figure 14 shows the computed Gibbs energies with respect to the 0 K static energy of structure #23 as a function of temperature for structures #7 (found in experiments) and #23 (*ab initio* lowest-energy state at 0 K found in the present study). Even up to 600 K, i.e., slightly lower than the temperature above which the initial phase is not stable (Appendix E in the Supporting Information), the experimental

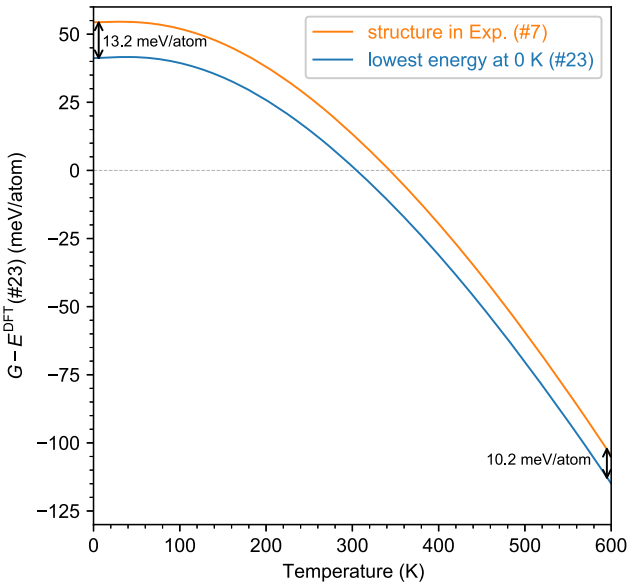

Figure 14. Computed Gibbs energies as a function of temperature of the Li_5Sn structures found in experiments (#7) and of *ab initio* lowest-energy states at 0 K (#23) in the present study using MTP-assisted *ab initio* thermodynamic integration with 288-atom supercell models. The 0 K static energy of structure #23 is set as a reference.

structure (#7) is found to be higher in Gibbs energy than structure #23, although the difference of the Gibbs energies becomes marginally smaller at higher temperatures. It should be emphasized that the Gibbs energy in the present approach considers full vibrational anharmonicity and the coupling between the lattice vibrations and electronic excitations. This implies that the experimental *Cmcm* Li_5Sn structure is realized, not due to thermodynamic stabilization but likely due to kinetic reasons, e.g., due to the cooling process from the liquid phase.

5. CONCLUSIONS

For the binary system Li−Sn, a new and to date the most lithium-rich compound Li_5Sn with the space group *Cmcm* was obtained and structurally characterized. Knowledge of the phase space is of pivotal importance for a deeper understanding of the electrode processes in the lithium−tin battery. Formation of this particular lithium-rich compound would enable an increase of the capacity. In accordance with two independent recent predictions, the crystal structure is composed of the identical coordination polyhedra (notably bicapped hexagonal prisms around Sn and Li(1) and Edshammer polyhedra around Li(2)) though differently arranged.

Ab initio analyses, including thermodynamic integration using Langevin dynamics in combination with moment tensor potentials, have also been conducted to understand the thermodynamic stability of the experimentally observed *Cmcm* Li_5Sn structure. Among the 108 Li_5Sn structures systematically derived using the structure enumeration algorithm,[36,37] including the *Cmcm* structure and those predicted in previous studies, another new structure with the space group type *Immm* has been found to be energetically the most stable at 0 K. This computationally found *Immm* structure is thermodynamically favorable even at finite temperatures, indicating that the experimentally observed

https://doi.org/10.1021/jacs.1c10640
J. Am. Chem. Soc. 2022, 144, 7096−7110

Cmcm Li_5Sn is realized due to kinetics rather than thermodynamics.

■ ASSOCIATED CONTENT

Supporting Information

The Supporting Information is available free of charge at https://pubs.acs.org/doi/10.1021/jacs.1c10640.

> Displacement parameters of experimentally found *Cmcm* Li_5Sn, further details of the computational conditions of the Gibbs energies at finite temperatures, comparison of the *ab initio* structural parameters of *P6/mmm* (#0) and *C2/m* (#83) Li_5Sn with previous publications, *ab initio* structural stability of *Cmcm* (#7) and *Immm* (#23) Li_5Sn at finite temperatures using MTPs, density of states of *Cmcm* (#7) Li_5Sn (PDF)

Accession Codes

CCDC 2099217 contains the supplementary crystallographic data for this paper. These data can be obtained free of charge via www.ccdc.cam.ac.uk/data_request/cif, or by emailing data_request@ccdc.cam.ac.uk, or by contacting The Cambridge Crystallographic Data Centre, 12 Union Road, Cambridge CB2 1EZ, UK; fax: +44 1223 336033.

■ AUTHOR INFORMATION

Corresponding Author

Yuji Ikeda − *Institute for Materials Science, University of Stuttgart, 70569 Stuttgart, Germany;* orcid.org/0000-0001-9176-3270; Email: yuji.ikeda@imw.uni-stuttgart.de

Authors

Robert U. Stelzer − *Institute of Inorganic Chemistry, University of Stuttgart, 70569 Stuttgart, Germany*

Prashanth Srinivasan − *Institute for Materials Science, University of Stuttgart, 70569 Stuttgart, Germany;* orcid.org/0000-0002-9199-4340

Tanja S. Lehmann − *Institute of Inorganic Chemistry, University of Stuttgart, 70569 Stuttgart, Germany*

Blazej Grabowski − *Institute for Materials Science, University of Stuttgart, 70569 Stuttgart, Germany;* orcid.org/0000-0003-4281-5665

Rainer Niewa − *Institute of Inorganic Chemistry, University of Stuttgart, 70569 Stuttgart, Germany;* orcid.org/0000-0002-2633-7109

Complete contact information is available at: https://pubs.acs.org/10.1021/jacs.1c10640

Notes

The authors declare no competing financial interest.

■ ACKNOWLEDGMENTS

This project has received funding from the European Research Council (ERC) under the European Union's Horizon 2020 research and innovation programme (grant agreement no. 865855). The authors also acknowledge support by the state of Baden-Württemberg through bwHPC and the DFG through grant no. INST 40/467-1 FUGG (JUSTUS cluster) and the support by the Stuttgart Center for Simulation Science (SimTech). P.S. would like to thank the Alexander von Humboldt Foundation for their support through the Alexander von Humboldt Postdoctoral Fellowship Program.

■ REFERENCES

(1) Ma, D.; Cao, Z.; Hu, A. Si-based anode materials for Li-ion batteries: A mini review. *Nano-Micro Lett.* **2014**, *6*, 347−358.

(2) Korthauer, R., Ed. *Handbuch Lithium-Ionen-Batterien*; Springer Berlin Heidelberg, 2013.

(3) Teki, R.; Datta, M. K.; Krishnan, R.; Parker, T. C.; Lu, T.-M.; Kumta, P. N.; Koratkar, N. Nanostructured silicon anodes for lithium ion rechargeable batteries. *Small* **2009**, *5*, 2236−2242.

(4) Sun, P.; Davis, J.; Cao, L.; Jiang, Z.; Cook, J. B.; Ning, H.; Liu, J.; Kim, S.; Fan, F.; Nuzzo, R. G.; Braun, P. V. High capacity 3D structured tin-based electroplated Li-ion battery anodes. *Energy Storage Mater.* **2019**, *17*, 151−156.

(5) Winter, M.; Besenhard, J. O.; Spahr, M. E.; Novák, P. Insertion electrode materials for rechargeable lithium batteries. *Adv. Mater.* **1998**, *10*, 725−763.

(6) Masing, G.; Tammann, G. Über das Verhalten von Lithium zu Natrium, Kalium, Zinn, Cadmium und Magnesium. *Z. Anorg. Chem.* **1910**, *67*, 183−199.

(7) Gladyshevskii, E. I.; Oleksiv, G. I.; Kripyakevich, P. I. New examples of the structural type $Li_{22}Pb_5$. *Kristallografiya* **1964**, *9*, 338−341.

(8) Baroni, A. Alloys of Li. thermal and X-ray analysis of the system Li-Sn. *Atti Rend. Accad. Lincei, Roma* **1932**, *16*, 153−158.

(9) Sangster, J.; Bale, C. W. The Li-Sn (lithium-tin) system. *J. Phase Equilibria Diffus* **1998**, *19*, 70−75. Li, D.; Fürtauer, S.; Flandorfer, H.; Cupid, D. M. Thermodynamic assessment and experimental investigation of the Li−Sn system. *Calphad* **2014**, *47*, 181−195.

(10) Grube, O.; Meyer, E. Elektrische Leitfähigkeit und Zustandsdiagramm bei binären Legierungen. *Z. Elektrochem. Angew. Phys. Chem.* **1934**, *40*, 771−777.

(11) Frank, U.; Müller, W.; Schäfer, H. Die Kristallstruktur der Phase Li_7Sn_2/the crystal structure of Li_7Sn_2. *Z. Naturforsch. B* **1975**, *30*, 6−9.

(12) Frank, U.; Müller, W.; Schäfer, H. Die Struktur der Phase Li_5Sn_2/the crystal structure of Li_5Sn_2. *Z. Naturforsch. B* **1975**, *30*, 1−5.

(13) Müller, W.; Schäfer, H. Die Kristallstruktur der Phase LiSn. *Z. Naturforsch. B* **1973**, *28*, 246−248.

(14) Müller, W. Darstellung und struktur der phase Li_7Sn_3/preparation und crystal structure of Li_7Sn_3. *Z. Naturforsch. B* **1974**, *29*, 304−311.

(15) Hansen, D. A.; Chang, L. J. Crystal structure of Li_2Sn_5. *Acta Crystallogr.* **1969**, *B25*, 2392−2395.

(16) Frank, U.; Müller, W. Darstellung und Struktur der Phase $Li_{13}Sn_5$ und die strukturelle Verwandtschaft der Phasen in den Systemen Li−Sn und Li−Pb. *Z. Naturforsch. B* **1975**, *30*, 316−322.

(17) Blase, W.; Cordier, G. Crystal structure of β-lithium stannide, β-LiSn. *Z. Kristallogr. Cryst. Mater.* **1990**, *193*, 317−318.

(18) Gasior, W.; Moser, Z.; Zakulski, W. Thermodynamic studies and the phase diagram of the Li−Sn system. *J. Non-Cryst. Solids* **1996**, *205−207*, 379−382.

(19) Goward, G. R.; Taylor, N. J.; Souza, D. C. S.; Nazar, L. F. The true crystal structure of $Li_{17}M_4$ (M = Ge, Sn, Pb)−revised from $Li_{22}M_5$. *J. Alloys Compd.* **2001**, *329*, 82−91.

(20) Lupu, C.; Mao, J.-G.; Rabalais, J. W.; Guloy, A. M.; Richardson, J. W. X-ray and neutron diffraction studies on "$Li_{4.4}Sn$. *Inorg. Chem.* **2003**, *42*, 3765−3771.

(21) Tsuji, Y.; Hashimoto, W.; Yoshizawa, K. Lithium-richest phase of lithium tetrelides $Li_{17}Tt_4$ (Tt = Si, Ge, Sn, and Pb) as an electride. *Bull. Chem. Soc. Jpn.* **2019**, *92*, 1154−1169.

(22) Reichmann, T. L.; Gebert, C.; Cupid, D. M. Investigation of the Li solubility in the intermediate phase $Li_{17}Sn_4$ relevant to understanding lithiation mechanisms in Sn-based anode materials. *J. Alloys Compd.* **2017**, *714*, 593−602.

(23) Foster, M. S.; Crouthamel, C. E.; Wood, S. E. Thermodynamics of binary alloys. II. the lithium−tin system. *J. Phys. Chem.* **1966**, *70*, 3042−3045.

(24) Frerichs, J. E.; Koppe, J.; Engelbert, S.; Heletta, L.; Brunklaus, G.; Winter, M.; Madsen, G. K. H.; Hansen, M. R. ^{119}Sn and ^{7}Li solid-state NMR of the binary Li−Sn intermetallics: Structural finger-

printing and impact on the isotropic ^{119}Sn shift via DFT calculations. *Chem. Mater.* **2021**, *33*, 3499−3514.
(25) Sen, R.; Johari, P. Understanding the lithiation of the Sn anode for high-performance Li-ion batteries with exploration of novel Li−Sn compounds at ambient and moderately high pressure. *ACS Mater. Inter.* **2017**, *9*, 40197−40206.
(26) Mayo, M.; Morris, A. J. Structure prediction of Li−Sn and Li−Sb intermetallics for lithium-ion batteries anodes. *Chem. Mater.* **2017**, *29*, 5787−5795. Mayo, M.; Darby, J. P.; Evans, M. L.; Nelson, J. R.; Morris, A. J. Correction to structure prediction of Li−Sn and Li−Sb intermetallics for lithium-ion batteries anodes. *Chem. Mater.* **2018**, *30*, 5516−5517.
(27) Sheldrick, G. M. SHELXT — integrated space-group and crystal-structure determination. *Acta Crystallogr.* **2015**, *A71*, 3−8.
(28) Momma, K.; Izumi, F. *VESTA*3 for three-dimensional visualization of crystal, volumetric and morphology data. *J. Appl. Crystallogr.* **2011**, *44*, 1272−1276.
(29) Patterson, A. L.; Love, W. E. Remarks on the Delaunay reduction. *Acta Crystallogr.* **1957**, *10*, 111−116.
(30) Aroyo, M. I., Ed. *International Tables for Crystallography Vol. A: Space-group symmetry*, 6th ed.; International Union of Crystallography, 2016.
(31) Pickard, C. J.; Needs, R. J. High-pressure phases of silane. *Phys. Rev. Lett.* **2006**, *97*, 045504.
(32) Pickard, C. J; Needs, R J *Ab initio* random structure searching. *J. Phys.: Condens. Matter* **2011**, *23*, 053201.
(33) Oganov, A. R.; Glass, C. W. Crystal structure prediction using *ab initio* evolutionary techniques: Principles and applications. *J. Chem. Phys.* **2006**, *124*, 244704.
(34) Oganov, A. R.; Lyakhov, A. O.; Valle, M. How evolutionary crystal structure prediction works—and why. *Acc. Chem. Res.* **2011**, *44*, 227−237.
(35) Lyakhov, A. O.; Oganov, A. R.; Stokes, H. T.; Zhu, Q. New developments in evolutionary structure prediction algorithm USPEX. *Comput. Phys. Commun.* **2013**, *184*, 1172−1182.
(36) Hart, G. L. W.; Forcade, R. W. Algorithm for generating derivative structures. *Phys. Rev. B* **2008**, *77*, 224115.
(37) Hart, G. L. W.; Forcade, R. W. Generating derivative structures from multilattices: Algorithm and application to hcp alloys. *Phys. Rev. B* **2009**, *80*, 014120.
(38) Ångqvist, M.; Muñoz, W. A.; Rahm, J. M.; Fransson, E.; Durniak, C.; Rozyczko, P.; Rod, T. H.; Erhart, P. ICET — a python library for constructing and sampling alloy cluster expansions. *Adv. Theory Simul.* **2019**, *2*, 1900015.
(39) Grosse-Kunstleve, R. W.; Sauter, N. K.; Adams, P. D. Numerically stable algorithms for the computation of reduced unit cells. *Acta Crystallogr.* **2004**, *A60*, 1−6.
(40) Blöchl, P. E. Projector augmented-wave method. *Phys. Rev. B* **1994**, *50*, 17953−17979.
(41) Kresse, G.; Furthmüller, J. Efficient iterative schemes for *ab initio* total-energy calculations using a plane-wave basis set. *Phys. Rev. B* **1996**, *54*, 11169−11186.
(42) Kresse, G.; Furthmüller, J. Efficiency of *ab-initio* total energy calculations for metals and semiconductors using a plane-wave basis set. *Comput. Mater. Sci.* **1996**, *6*, 15−50.
(43) Kresse, G.; Joubert, D. From ultrasoft pseudopotentials to the projector augmented-wave method. *Phys. Rev. B* **1999**, *59*, 1758−1775.
(44) Methfessel, M.; Paxton, A. T. High-precision sampling for Brillouin-zone integration in metals. *Phys. Rev. B* **1989**, *40*, 3616−3621.
(45) Perdew, J. P.; Burke, K.; Ernzerhof, M. Generalized gradient approximation made simple. *Phys. Rev. Lett.* **1996**, *77*, 3865−3868.
(46) Ceperley, D. M.; Alder, B. J. Ground state of the electron gas by a stochastic method. *Phys. Rev. Lett.* **1980**, *45*, 566−569.
(47) Perdew, J. P.; Zunger, A. Self-interaction correction to density-functional approximations for many-electron systems. *Phys. Rev. B* **1981**, *23*, 5048−5079.
(48) Perdew, J. P.; Chevary, J. A.; Vosko, S. H.; Jackson, K. A.; Pederson, M. R.; Singh, D. J.; Fiolhais, C. Atoms, molecules, solids, and surfaces: Applications of the generalized gradient approximation for exchange and correlation. *Phys. Rev. B* **1992**, *46*, 6671−6687.
(49) Sun, J.; Ruzsinszky, A.; Perdew, J. P. Strongly constrained and appropriately normed semilocal density functional. *Phys. Rev. Lett.* **2015**, *115*, 036402.
(50) Sun, J.; Remsing, R. C.; Zhang, Y.; Sun, Z.; Ruzsinszky, A.; Peng, H.; Yang, Z.; Paul, A.; Waghmare, U.; Wu, X.; Klein, M. L.; Perdew, J. P. Accurate first-principles structures and energies of diversely bonded systems from an efficient density functional. *Nat. Chem.* **2016**, *8*, 831−836.
(51) Sanchez, J. M.; Ducastelle, F.; Gratias, D. Generalized cluster description of multicomponent systems. *Physica A* **1984**, *128*, 334−350.
(52) de Fontaine, D. Cluster approach to order-disorder transformations in alloys. In *Solid State Physics*, Vol. *47*; Academic Press: New York, 1994; pp 33−176.
(53) Ducastelle, F. Order and phase stability in alloys. In *Interatomic Potential and Structural Stability*; Terakura, K.; Akai, H., Eds.; Springer Berlin Heidelberg: Berlin, Heidelberg, 1993; pp 133−142.
(54) Tibshirani, R. Regression shrinkage and selection via the lasso. *J. R. Stat. Soc. B* **1996**, *58*, 267−288.
(55) Grabowski, B.; Ismer, L.; Hickel, T.; Neugebauer, J. *Ab initio* up to the melting point: Anharmonicity and vacancies in aluminum. *Phys. Rev. B* **2009**, *79*, 134106.
(56) Duff, A. I.; Davey, T.; Korbmacher, D.; Glensk, A.; Grabowski, B.; Neugebauer, J.; Finnis, M. W. Improved method of calculating *ab initio* high-temperature thermodynamic properties with application to ZrC. *Phys. Rev. B* **2015**, *91*, 214311.
(57) Beveridge, D. L.; DiCapua, F. M. Free energy via molecular simulation: Applications to chemical and biomolecular systems. *Annu. Rev. Biophys. Biophys. Chem.* **1989**, *18*, 431−492.
(58) Frenkel, D. *Understanding Molecular Simulation: From Algorithms to Applications*, 2nd ed.; Academic Press: San Diego, 2002.
(59) Alfè, D.; Price, G. D.; Gillan, M. J. Thermodynamics of hexagonal-close-packed iron under earth's core conditions. *Phys. Rev. B* **2001**, *64*, 045123.
(60) Zwanzig, R. W. High-temperature equation of state by a perturbation method. I. nonpolar gases. *J. Chem. Phys.* **1954**, *22*, 1420−1426.
(61) Allen, M. P.; Tildesley, D. J. *Computer Simulation of Liquids*, 2nd ed.; Oxford University Press, 2017.
(62) Grabowski, B.; Hickel, T.; Neugebauer, J. Formation energies of point defects at finite temperatures. *Phys. Status Solidi B* **2011**, *248*, 1295−1308.
(63) Zhang, X.; Grabowski, B.; Hickel, T.; Neugebauer, J. Calculating free energies of point defects from *ab initio*. *Comput. Mater. Sci.* **2018**, *148*, 249−259.
(64) Zhang, X.; Grabowski, B.; Körmann, F.; Ruban, A. V.; Gong, Y.; Reed, R. C.; Hickel, T.; Neugebauer, J. Temperature dependence of the stacking-fault Gibbs energy for Al, Cu, and Ni. *Phys. Rev. B* **2018**, *98*, 224106.
(65) Zhu, L.-F.; Körmann, F.; Ruban, A. V.; Neugebauer, J.; Grabowski, B. Performance of the standard exchange-correlation functionals in predicting melting properties fully from first principles: Application to Al and magnetic Ni. *Phys. Rev. B* **2020**, *101*, 144108.
(66) Zhu, L.-F.; Janssen, J.; Ishibashi, S.; Körmann, F.; Grabowski, B.; Neugebauer, J. A fully automated approach to calculate the melting temperature of elemental crystals. *Comput. Mater. Sci.* **2021**, *187*, 110065.
(67) Mermin, N. D. Thermal properties of the inhomogeneous electron gas. *Phys. Rev.* **1965**, *137*, A1441−A1443.
(68) Zhang, X.; Grabowski, B.; Körmann, F.; Freysoldt, C.; Neugebauer, J. Accurate electronic free energies of the 3*d*, 4*d*, and 5*d* transition metals at high temperatures. *Phys. Rev. B* **2017**, *95*, 165126.
(69) Hellman, O.; Abrikosov, I. A.; Simak, S. I. Lattice dynamics of anharmonic solids from first principles. *Phys. Rev. B* **2011**, *84*, 180301.

https://doi.org/10.1021/jacs.1c10640
J. Am. Chem. Soc. 2022, 144, 7096−7110

(70) Hellman, O.; Steneteg, P.; Abrikosov, I. A.; Simak, S. I. Temperature dependent effective potential method for accurate free energy calculations of solids. *Phys. Rev. B* **2013**, *87*, 104111.
(71) Grabowski, B.; Ikeda, Y.; Srinivasan, P.; Körmann, F.; Freysoldt, C.; Duff, A. I.; Shapeev, A.; Neugebauer, J. Ab initio vibrational free energies including anharmonicity for multicomponent alloys. *npj Comput. Mater.* **2019**, *5*, 80.
(72) Shapeev, A. V. Moment tensor potentials: A class of systematically improvable interatomic potentials. *Multiscale Model. Simul.* **2016**, *14*, 1153−1173.
(73) Gubaev, K.; Podryabinkin, E. V.; Shapeev, A. V. Machine learning of molecular properties: Locality and active learning. *J. Chem. Phys.* **2018**, *148*, 241727.
(74) Gubaev, K.; Podryabinkin, E. V.; Hart, G. L.W.; Shapeev, A. V. Accelerating high-throughput searches for new alloys with active learning of interatomic potentials. *Comput. Mater. Sci.* **2019**, *156*, 148−156.
(75) Gubaev, K. *Machine-learning interatomic potentials for multi-component alloys*. Ph.D. thesis, Skolkovo Institute of Science and Technology, 2019.
(76) Ferrari, A.; Dutta, B.; Gubaev, K.; Ikeda, Y.; Srinivasan, P.; Grabowski, B.; Körmann, F. Frontiers in atomistic simulations of high entropy alloys. *J. Appl. Phys.* **2020**, *128*, 150901.
(77) Novikov, I. S; Gubaev, K.; Podryabinkin, E. V; Shapeev, A. V The MLIP package: moment tensor potentials with MPI and active learning. *Mach. Learn.: Sci. Technol.* **2021**, *2*, 025002.
(78) Podryabinkin, E. V.; Shapeev, A. V. Active learning of linearly parametrized interatomic potentials. *Comput. Mater. Sci.* **2017**, *140*, 171−180.
(79) Novikov, I. S.; Suleimanov, Y. V.; Shapeev, A. V. Automated calculation of thermal rate coefficients using ring polymer molecular dynamics and machine-learning interatomic potentials with active learning. *Phys. Chem. Chem. Phys.* **2018**, *20*, 29503−29512.
(80) Kanatzidis, M. G.; Pöttgen, R.; Jeitschko, W. The metal flux: A preparative tool for the exploration of intermetallic compounds. *Angew. Chem., Int. Ed.* **2005**, *44*, 6996−7023.
(81) Grüttner, A.; Nesper, R.; von Schnering, H. G. Novel metastable germanium modifications *allo*-Ge and 4H-Ge from Li_7Ge_{12}. *Angew. Chem., Int. Ed. Engl.* **1982**, *21*, 912−913.
(82) Kiefer, F.; Hlukhyy, V.; Karttunen, A. J.; Fässler, T. F.; Gold, C.; Scheidt, E.-W.; Scherer, W.; Nylén, J.; Häussermann, U. Synthesis, structure, and electronic properties of 4*H*-germanium. *J. Mater. Chem.* **2010**, *20*, 1780.
(83) Guloy, A. M.; Ramlau, R.; Tang, Z.; Schnelle, W.; Baitinger, M.; Grin, Y. A guest-free germanium clathrate. *Nature* **2006**, *443*, 320−323.
(84) Böhme, B.; Guloy, A.; Tang, Z.; Schnelle, W.; Burkhardt, U.; Baitinger, M.; Grin, Y. Oxidation of M_4Si_4 (M = Na, K) to clathrates by HCl or H_2O. *J. Am. Chem. Soc.* **2007**, *129*, 5348−5349.
(85) Edshammar, L.-E. *X-ray studies on binary alloys of aluminium with platinum metals*. Ph.D. thesis, Stockholm University, 1969.
(86) Lidin, S.; Popp, T.; Somer, M.; von Schnering, H. G. Generalized Edshammar polyhedra for the description of a family of solid-state structures. *Angew. Chem., Int. Ed.* **1992**, *31*, 924−927.
(87) Grabowski, B.; Hickel, T.; Neugebauer, J. *Ab initio* study of the thermodynamic properties of nonmagnetic elementary fcc metals: Exchange-correlation-related error bars and chemical trends. *Phys. Rev. B* **2007**, *76*, 024309.
(88) Paier, J.; Marsman, M.; Hummer, K.; Kresse, G.; Gerber, I. C.; Ángyán, J. G. Screened hybrid density functionals applied to solids. *J. Chem. Phys.* **2006**, *124*, 154709.
(89) Vinet, P.; Smith, J. R.; Ferrante, J.; Rose, J. H. Temperature effects on the universal equation of state of solids. *Phys. Rev. B* **1987**, *35*, 1945−1953.
(90) Otero-de-la-Roza, A.; Luaña, V. Gibbs2: A new version of the quasi-harmonic model code. I. robust treatment of the static data. *Comput. Phys. Commun.* **2011**, *182*, 1708−1720.

https://doi.org/10.1021/jacs.1c10640
J. Am. Chem. Soc. 2022, 144, 7096−7110